

RESEARCH ARTICLE

10.1002/2017JA024573

MLT Plasmopause Characteristics: Comparison Between THEMIS Observations and Numerical Simulations

Key Points:

- Formation (radial movement) of the main plasmopause (PP) is triggered between 21 and 07 MLT with the highest probability at postmidnight
- Main PP moves azimuthally with the velocity close to corotational one
- Main PP characteristics inferred from THEMIS measurements and from model predictions based on interchange mechanism are in agreement

Correspondence to:

M. Bandić,
mario.bandic.1@gmail.com

Citation:

Verbanac, G., Bandić, M., Pierrard, V., & Cho, J. (2018). MLT plasmopause characteristics: Comparison between THEMIS observations and numerical simulations. *Journal of Geophysical Research: Space Physics*, 123, 2000–2017. <https://doi.org/10.1002/2017JA024573>

Received 8 JUL 2017

Accepted 15 JAN 2018

Accepted article online 18 JAN 2018

Published online 30 MAR 2018

Giuli Verbanac¹ , Mario Bandić² , Viviane Pierrard^{3,4} , and Junghee Cho⁵

¹Department of Geophysics, Faculty of Science, University of Zagreb, Zagreb, Croatia, ²Zagreb Astronomical Observatory, Zagreb, Croatia, ³Royal Belgian Institute for Space Aeronomy (Space Physics and STCE), Brussels, Belgium, ⁴Earth and Life Institute, TECLIM, Université Catholique de Louvain, Louvain-La-Neuve, Belgium, ⁵Department of Astronomy and Space Science, Chungbuk National University, Cheongju, South Korea

Abstract We perform a statistical comparison of the global behavior of the THEMIS observed and simulated plasmopause in the geomagnetic equatorial plane. Simulation is based on the interchange instability mechanism. Analyzing plasmopause positions (L_{PPS}) from the period July 2008 to December 2012, we derived formation and propagation characteristics of the main plasmopause, which reflect the most probable global plasmopause behavior. The results suggest a global eastward azimuthal plasmopause propagation and a radial plasmopause motion limited to the 21–07 MLT sector. The formation of the plasmopause takes place with the highest probability at postmidnight. It is likely that the erosion occurs in a range of MLTs simultaneously. On the dayside, the plasmopause moves almost entirely azimuthally. We suggest that the plasmopause propagates azimuthally with a mean angular velocity close to the corotation speed at all MLTs, at least during periods of lower geomagnetic activity. The results also show that the experimental plasmopause characteristics are in accordance with the interchange instability mechanism. Along with the proposed suggestions for future works, this study contributes to making a further step toward resolving some of the long-lasting, unresolved issues related to plasmopause dynamics.

1. Introduction

Plasmopause is the outer boundary of the plasmasphere where the plasma characteristics change abruptly. Since the plasma behaviors influence the inner magnetosphere (e.g., ring current and radiation belts), it is important to know the location of the plasmopause as a function of time, thus, to understand physical processes responsible for the plasmopause formation and evolution.

The novel missions, IMAGE, CLUSTER, and THEMIS have given a new insight into the plasmaspheric dynamics and have revealed different unexpected plasmopause structures (e.g., plumes, notches, and shoulders) that are mainly formed during the periods of enhanced geomagnetic activities. These data along with data from ISEE and CRRES satellites have allowed for better understanding of the plasmasphere dynamics.

Relationships between plasmopause positions (L_{PPS}) and/or solar wind parameters/geomagnetic indices obtained with statistical studies (Bandić et al., 2016; Carpenter & Anderson, 1992; Liu et al., 2015; Moldwin et al., 2002; O'Brien & Moldwin, 2003; Verbanac et al., 2015) have provided the plasmopause shapes for different levels of geomagnetic indices. Many works have also been focused on studying specific events, usually related to geomagnetic storms and, in general, were successful in explaining the observed plasmopause features (e.g., Goldstein, Burch, et al., 2005; Goldstein, Sandel, et al., 2005; Pierrard & Cabrera, 2005; Pierrard et al., 2008).

Although great progress has been made in understanding the plasmaspheric evolution and plasmopause structure formation, the question of what causes erosion of the plasmasphere has still remained unanswered.

MHD models that have been used to study the plasmopause dynamics assume that the plasmopause corresponds to the Last Closed Equipotential (LCE) of a stationary magnetospheric electric field (E field) or to the Last Closed Streamline (LCS) of the time-dependent magnetospheric convection. The positions of the LCS depend on the simulation initial conditions (e.g., the specification of initial plasmopause boundary or the assumed simulation closure time). Initial plasmopause can be inferred from global plasmopause snapshot,

for example, IMAGE EUV plasmopause images (Goldstein et al., 2002). Different simulation closure time gives different plasmopause positions (Chen & Wolf, 1972; Lemaire & Pierrard, 2008). In the alternative theory for the plasmopause formation, the theory of the interchange instability mechanism (Lemaire & Kowalkowski, 1981; Lemaire & Gringauz, 1998), the plasmopause is identified with a streamline tangent to the Zero Parallel Force surface (ZPFS) where the field-aligned component of the centrifugal and gravitational acceleration balance each other. Above this surface, the plasma becomes unstable at postmidnight where the convection electric field has the largest value. Additionally, in the postmidnight sector, the interchange velocity is the largest and that causes the maximal erosion in these MLT sectors. Note that interchange velocity is proportional to the centrifugal acceleration and inversely proportional to the Pedersen conductivity which are maximal/minimal in postmidnight MLTs (see equation (2) in Lemaire & Kowalkowski, 1981). The interchange instability mechanism enables not only to follow the plasmopause evolution but also to study the initial plasmopause formation. Plasmopause position can be obtained just by knowing the geomagnetic activity during the previous 24 h; thus, these simulations are not dependent on the assumptions taken at the initial time of the simulation. For more details on these two physical mechanisms and their comparison the readers are referred to the works by Lemaire and Pierrard (2008) and Pierrard et al. (2008).

Both of these theories have been quite successful in reproducing many different plasmopause structures (e.g., notches, shoulders, and plumes) observed by EUV on IMAGE. However, direct comparison between these theoretical models and EUV images performed for particular events have shown that none of the available E field models allows for simulating in detail all of the plasmopause features. Usually, the electric field has to be modified to obtain exactly what is observed in specific events. For instance, Goldstein et al. (2003) included an additional E field distribution in their model related to subauroral polarization stream (SAPS) to obtain a better fit between the observations of EUV IMAGE (2 June 2001 event) and the results of LCS simulations. Pierrard et al. (2008) suggested that the effect of induced electric fields generated during the intense geomagnetic storms caused the discrepancy between EUV observations and interchange instability simulations with the ESD electric field for two studied storm events (8 October 2001 and 17 April 2002 events). More recently, Murakami et al. (2016) have analyzed the first global meridian images of the plasmasphere (1–2 May 2008 event) obtained with KAGUYA/TEX instrument. They showed that the plasmopause positions at the postmidnight side observed from the meridian perspective are in agreement with those derived using the dynamic simulations based on the interchange mechanism, with a plasmopause formation first near the equatorial region.

Lately, Bandić et al. (2017) have indicated the great need for statistical comparison of observed L_{pp} s with MHD models, which include convection, rotation, and SAPS, and with simulations based on interchange instability motion. In the present study, we focus on the latter suggestion, since simulations including interchange are accessible to any user for a free run on the space weather portal (<https://www.spaceweather.eu>). We have derived simulated L_{pp} s (thereafter sL_{pp} s) taking into account interchange instability mechanism. The response of sL_{pp} s to solar wind/geomagnetic activity indices (thereafter PP indicators) at different MLTs is compared with the response inferred from experimental THEMIS-based L_{pp} s (thereafter eL_{pp} s) which embrace period 2008–2012.

Note that in the present study, for the first time, the theoretical results are compared with large statistical plasmopause sample. The great advantage of our approach and statistical analysis (explained in the next section) is that it (i) allows to investigate global processes of plasmopause formation and propagation that are still not well understood despite new insights obtained in last decade; (ii) allows to derive global plasmopause characteristics by using plasmopause positions obtained over the large time period, although for any chosen date THEMIS measurements do not provide eL_{pp} s in all MLTs for every UT hour; (iii) does not require sequences of plasmopause images; (iv) can show the most important physical effects on plasmopause formation and propagation. In such a way, our study contributes to constraining the physical mechanism by which the formation of the main plasmopause is triggered.

In the next section, we introduce the data sets and methods used for the analyses. Characteristics and comparison of the employed data sets are given in section 3. In section 4 we present and discuss the obtained MLT dependence of the simulated plasmopause, which is then compared with THEMIS observations in section 5. Discussions and conclusions are given in sections 6 and 7, respectively.

2. Data and Method

The following data sets are used for the period 2008–2012: (1) THEMIS-based L_{pp} s (eL_{pp} s); (2) L_{pp} s obtained from numerical simulations based on the interchange instability mechanism (sL_{pp} s); (3) hourly values of geomagnetic indices AE (auroral electrojet index) and Dst (storm time disturbance index), and 3-hourly values of Ap (planetary geomagnetic activity index); (4) hourly values of solar wind parameters: velocity V , southward component of the interplanetary magnetic field (IMF) vector B_s (B_s is zero for $B_z > 0$, B_z is the z component of the IMF vector in Geocentric Solar Magnetospheric coordinate frame), $B_s V$ related to the y component of interplanetary electric field vector, and the Newell function (Newell et al., 2007) that includes different physical processes responsible for the magnetospheric activity such as the rate at which IMF field lines are convected toward the magnetopause, the fraction of field lines merge, the length of the merging line, and the amount of the opened flux. More details on importance of this solar wind coupling function (here PP indicator) are given in Verbanac et al. (2015) and Bandić et al. (2016);

We used the same 6,840 eL_{pp} s as in Bandić et al. (2017), which are obtained from measurements of the electric field instrument (EFI) and the electrostatic analyzer (ESA) on board THEMIS A, D, and E satellites. They define the plasmopause as the innermost sharp density gradient (dn/dr where n is density and r is radial distance) of at least a factor of 15 within a radial distance of $0.5 R_E$. To distinguish the plasmasphere from the possible significant density structures outside the plasmopause (indicated by, e.g., Gallagher et al., 2005; Horwitz et al., 1990; Sandel et al., 2003; Sheeley et al., 2001), they required an additional condition that the density level itself prior to the drop is $\geq 100/\text{cm}^3$ at all L shells. More details about the plasmopause identification are given in Cho et al. (2015).

The second L_{pp} data set is derived from numerical simulations based on interchange instability mechanism available at the space weather portal (<https://www.spaceweather.eu>) (Pierrard & Lemaire, 2004; Pierrard & Stegen, 2008). The program retrieves the geomagnetic index Kp for any chosen date and time (T_0) and of the preceding day. Then, the position of the plasmopause is calculated, assuming the corotation, the Kp -dependent convection electric field model E5D (McIlwain, 1986), and the associated magnetic field model. In the simulations, plasma elements with density smaller than the background density are launched in the equatorial plane. Due to the interchange motion, these elements automatically go to the ZPFS and after about 24 h, the plasmopause values are stable and are not dependent on any initial conditions. Thus, the plasmopause at any chosen time is determined by the interchange mechanism and by the history of geomagnetic activity during the previous 24 h. Simulations start at 02 MLT because the ZPFS penetrates to the lowest radial distance around that MLT due to the largest E5D values there (see, e.g., Figure 2 in Lemaire & Pierrard, 2008). For each simulation, we have chosen the input ionospheric velocity to be that of the corotation. We perform the simulations for randomly taken 68 days within the studied time span. At least 1 day per month is considered. For each day, at all UT hours, one sL_{pp} within each 1 h MLT bin is randomly extracted resulting in 600 sL_{pp} s per day (24 MLT \times 25 UT). Note that we have 25 UT hours within 1 day, because we consider the 00 UT of the first day and 00 UT of the second day as well. Thus, simulations have perfect UT-MLT coverage (1 h space-time resolution: space resolution of 1 h bin MLT, 1 h UT time resolution). More about the characteristics of this data set is given in the next section.

As an example of the simulation output, in Figure 1 we present plasmopause in the geomagnetic equatorial plane at five instants of time of 9 August 2008. This chosen date that starts at $T_0 = 00:00$ UT is denoted as “day 2” as the Kp history of the previous 24 h is taken into account.

The time difference between each panel is 2 h. The geomagnetic Kp index is also displayed. As can be seen in this figure, the simulation does not stop after one full cycle at 02 MLT but continues farther up to 05 MLT. Thus, each simulation covers 27 MLTs providing two sL_{pp} branches between 02 MLT and 05 MLT. Therefore, the largest possible number of sL_{pp} s per simulation is 675 (27 MLTs \times 25 UTs). However, we were not able to retrieve all the potential sL_{pp} s in every simulation due to the occasional gaps in the plasmopause. Gaps are caused by the loss of some of the plasma elements at large Kp jumps (e.g., sudden increase from $Kp = 3$ to $Kp = 5$), while in the case of $Kp = 0$, no sL_{pp} at all can be inferred from the simulation. We develop the data set which contains 41,113 sL_{pp} s. In the following the branch from 02 MLT to 02 MLT is referred as the first simulation cycle, and the branch 02–05 MLT is referred as the second simulation cycle. Note that the branch related to the second simulation cycle is farther from the planet when Kp increases (as in the shown example), but is closer to the Earth when Kp decreases. This is related to plasmopause formation and is explained in more detail in section 4.

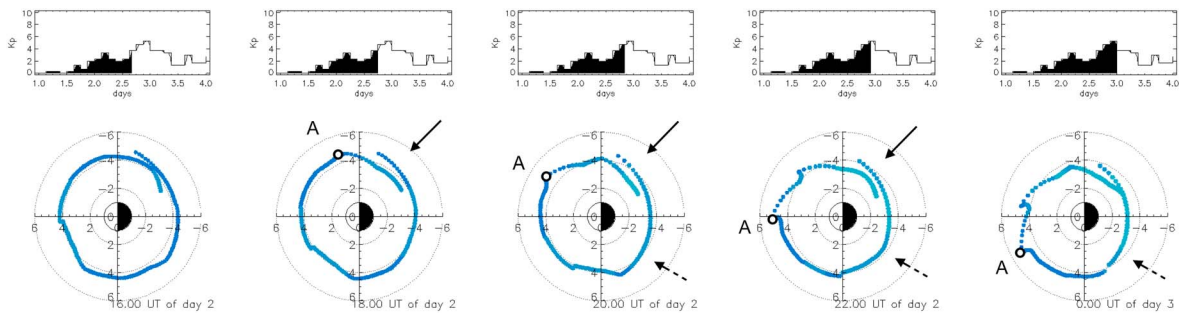


Figure 1. An example of the simulation output: plasmopause at five different UT of 9 August 2008 and the K_p index. For more details see text.

The response of the simulated plasmopause to various PP indicators at different MLTs is investigated by applying the cross-correlation (thereafter CC) analysis. The CC coefficients are obtained using the equation (10) given in Kwan (2009). All CC functions are derived up to a time lag (T_{lag}) of 30 h with a step of 1 h (the applied data resolution), the same as proposed by Verbanac et al. (2015). In the following, T_{lag} is referred to as the time the plasmasphere needs to react to the changes of the E field in the specific MLT sector. The initial T_{lag} is the time needed for the first plasmopause reaction to the changes in the E field (and additionally, the propagation time from the satellite to the magnetopause when solar wind data are used). The simulated sL_{pps} from the first and second simulation cycles are analyzed separately; thus, in sectors 02–05 MLT we have two different CC curves. The obtained results are discussed in section 4 and then the importance of considering the sL_{pps} from both cycles will become clear. The same analysis is made with experimental, THEMIS-based eL_{pps} , and then the comparison with theoretical CC curves is performed.

As in Bandić et al. (2017), to investigate the propagation of the plasmopause we use here the mean angular velocity defined as

$$\omega_{IM} = \frac{\Delta T_{resolution} [h]}{\Delta T_{lag} [h]} \quad (1)$$

where $\Delta T_{resolution}$ is the interval length of the MLT bin and ΔT_{lag} is the difference between the T_{lag} of the analyzed MLT bin and of the previous MLT bin. Since data are binned in 1 h MLT bins (00–01 MLT, 02–03 MLT, ..., 23–24 MLT) the $\Delta T_{resolution}$ is 1 h. The ω_{IM} is expressed as a fraction of the Earth's angular rotation speed.

3. Characteristics and Comparison of the Employed Data Sets

3.1. Characteristics of Experimental and Simulated Data Sets

In the studied period, THEMIS observed a plasmopause on average 4 times per day. For any hour of the chosen date, it is possible to obtain at most three eL_{pps} in some of the 1 h MLT bins due to the orbit constellations of THEMIS A, D, and E satellites. Consequently, we do not have a sequential time series of eL_{pps} . MLT distribution of the eL_{pps} is given in Bandić et al. (2017), Table 1.

The works by Verbanac et al. (2015), Bandić et al. (2016), and especially work by Bandić et al. (2017) based on different satellites (CLUSTER, CRRES, and THEMIS, respectively) have all distinguished the MLT sectors of the plasmopause formation and eastward plasmopause propagation. They examined the absolute maximum of the CC curves but did not investigate the systematic behavior of the curves. In the present work, we recognize that the whole THEMIS-based CC curves, not only the peak values, reflect the plasmaspheric dynamics. Consequently, we sought for the simulated data set that facilitates recognition of the observed plasmopause characteristics (as rotation and formation), which thus enables to obtain reliable CC curves. First, we perform the preliminary analysis with simulations. The sL_{pps} of individual events (as, e.g., the one shown in Figure 1) were inspected to check if the simulations reproduce the plasmopause characteristics indicated by the experimental data sets. All cases revealed MLT sectors of the plasmopause formation and eastward plasmopause rotation. To study these features statistically in detail, a data set that contains plasmapauses that are close both in time and space is the most favorable one. Therefore, we created the simulated data set extracting plasmopause from sequential UT snapshots with complete MLT coverage (as explained in the previous section). To obtain reliable CC curves we increased the amount of the data and repeated the simulation until the shape of the CC curves stopped to change. The analysis of such simulated data set can help to interpret the statistical

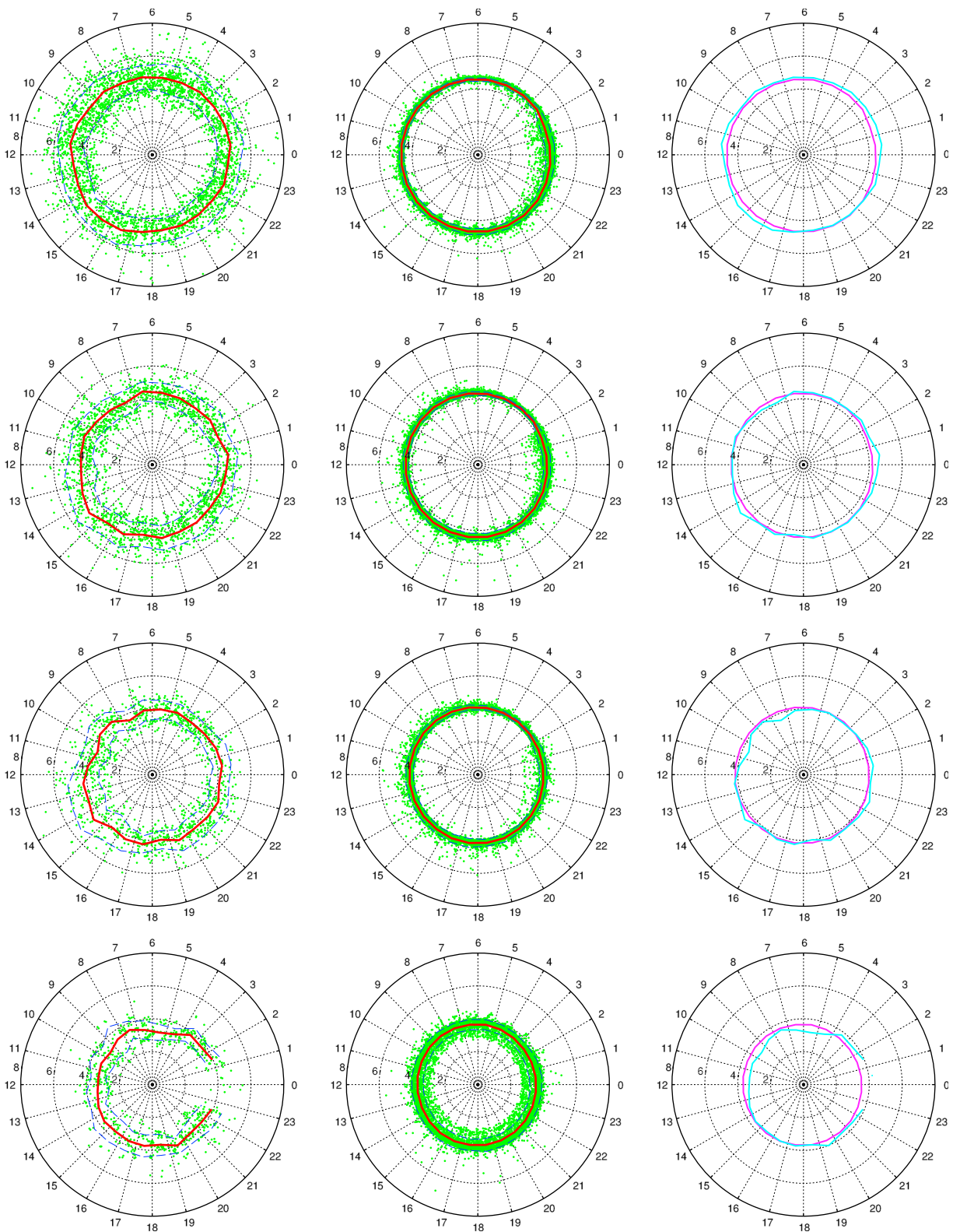


Figure 2. Location of the (left column) eL_{pp} s and (middle column) sL_{pp} s in 1 h MLT bins as a function of A_p is shown as green dots divided into four different A_p levels. Overlaid onto these figures are the mean of the plasmopause in each 1 h MLT bin (depicted as red) and the std (depicted as dashed blue). The mean eL_{pp} (depicted as greenish-blue) and sL_{pp} (depicted as purplish-red) locations are shown together in the right column.

results obtained from real observations. If we chose to extract the plasmopause at the times that are close to that of the experimental plasmopause (note that UT hour of the sL_{pp} and eL_{pp} can differ up to an hour, as the measurements are at an arbitrary time and the simulations at every full hour), we would indeed create the data set similar to CLUSTER, CRRES, and THEMIS data sets that all lack in ample and uniform MLT-UT data coverage. Thus, the CC curves derived using such simulated data set would be oscillatory and would not be stable. This issue is discussed in more detail in section 5.

3.2. Comparison of the Experimental and the Simulated Data Sets

In order to compare experimental and simulated plasmopause positions, which differ both in number and UT, we group the data according to the value of the A_p index. Data are divided into four levels of A_p : 0–4 (group I), 4–7 (group II), 7–15 (group III), >15 (group IV). Note that the A_p values are values at the strongest correlation in the interval of 30 h preceding the L_{pp} s. These values are generally lower than the maximum A_p values in the interval prior to L_{pp} s, which have been commonly used by previous modelers (e.g., Moldwin et al., 2002). The largest A_p values are $A_p = 207$ and $A_p = 111$ for simulated and for experimental data sets, respectively. Number of data within each group (from I to IV) is as follows: group I: 3,087 eL_{pp} s, 10,058 sL_{pp} s; group II: 1,976 eL_{pp} s, 11,774 sL_{pp} s; group III: 1,115 eL_{pp} s, 8,089 sL_{pp} s; group IV: 662 eL_{pp} s and 6,527 sL_{pp} s. As the geomagnetic activity level increases, the number of data decreases. A small exception is group II of the simulated data set which contains more data than group I. This occurred because the simulations are performed for randomly taken 68 days within the studied period. Note that group IV ($A_p > 15$) contains less than 10% of overall data for the experimental data set and less than 18% for the simulated data set. Moreover, within this group, the number of data further decreases as geomagnetic activity increases (e.g., for A_p values between 80 and $A_p = 111$, the experimental data set contains only nine eL_{pp} s). Thus, the majority of the plasmopause positions are related to the very low geomagnetic activity. Indeed, THEMIS data set includes only 30 moderate and 9 great storms.

Figure 2 (left and middle columns) examines how the location of the eL_{pp} s and sL_{pp} s (depicted as green dots) varies as a function of A_p and MLT. Overlaid onto these figures are the mean of the plasmopause in each 1 h MLT bin (depicted as red) and the standard deviations (thereafter std, depicted as dashed blue). The mean eL_{pp} and sL_{pp} locations are shown together in Figure 2 (right column). For a given level of A_p , the eL_{pp} is essentially circular as expected since most plasmopause positions are related to the very low geomagnetic activity. Namely, many studies have obtained plasmopause without pronounced bulge at the times of low geomagnetic activity (e.g., Bandić et al., 2016; Kwon et al., 2015; Liu & Liu, 2014; O'Brien & Moldwin, 2003). Simulations also give the circular sL_{pp} for a fixed geomagnetic activity level. Both eL_{pp} s and sL_{pp} s move closer to the Earth when A_p increases. When all MLT sectors are taken together, the mean eL_{pp} s are 4.8, 4.4, 4.1, and 3.6 for groups I–IV, respectively. The corresponding mean sL_{pp} s values amount for 4.6, 4.4, 4.1, and 3.7. The mean eL_{pp} s and sL_{pp} s are close to each other within each group. Note that the change of the activity level does not give a very large difference in the mean plasmopause, since the transitions between each level are actually very soft. The mean eL_{pp} and sL_{pp} in each MLT bin at all activity levels are also very close as can be seen in Figure 2 (right column). At all considered activity levels and at all MLTs the scatter about the mean (characterized by std) is larger for eL_{pp} than for sL_{pp} . Namely, when all MLT sectors are taken together the mean std for eL_{pp} s are 0.8, 0.7, 0.7, and 0.6 for groups I–IV, respectively. For sL_{pp} s the mean std values are 0.2 for groups I–III and 0.3 for group IV. For both eL_{pp} and sL_{pp} , there is no significant difference in the variability about the mean in different MLT sectors.

In summary, the simulation results are in agreement with the real data. Larger MLT-L scatter of the eL_{pp} may be in part due to the errors in the electric field instrument and the electrostatic analyzer measurements that lead to the uncertainty in eL_{pp} s determinations but can also mean that some other mechanisms (other than interchange) were acting and influencing the real data and that there are other parameters than A_p controlling the plasmopause. Note also that the simulated radial distance and the shape of the plasmopause depend on the used empirical convection electric field model (here E5D that uses the $Kp \sim A_p$ as the input parameter) that is only an approximation of the actual field distributions.

4. MLT Dependence of the Simulated Plasmopause

In this section, we discuss the CC functions obtained using simulated sL_{pp} s. In Figure 3 (first figure column or first two columns for sectors 02–05 MLTs) and Figure 4 (first two columns for sectors 02–05 MLTs) we show

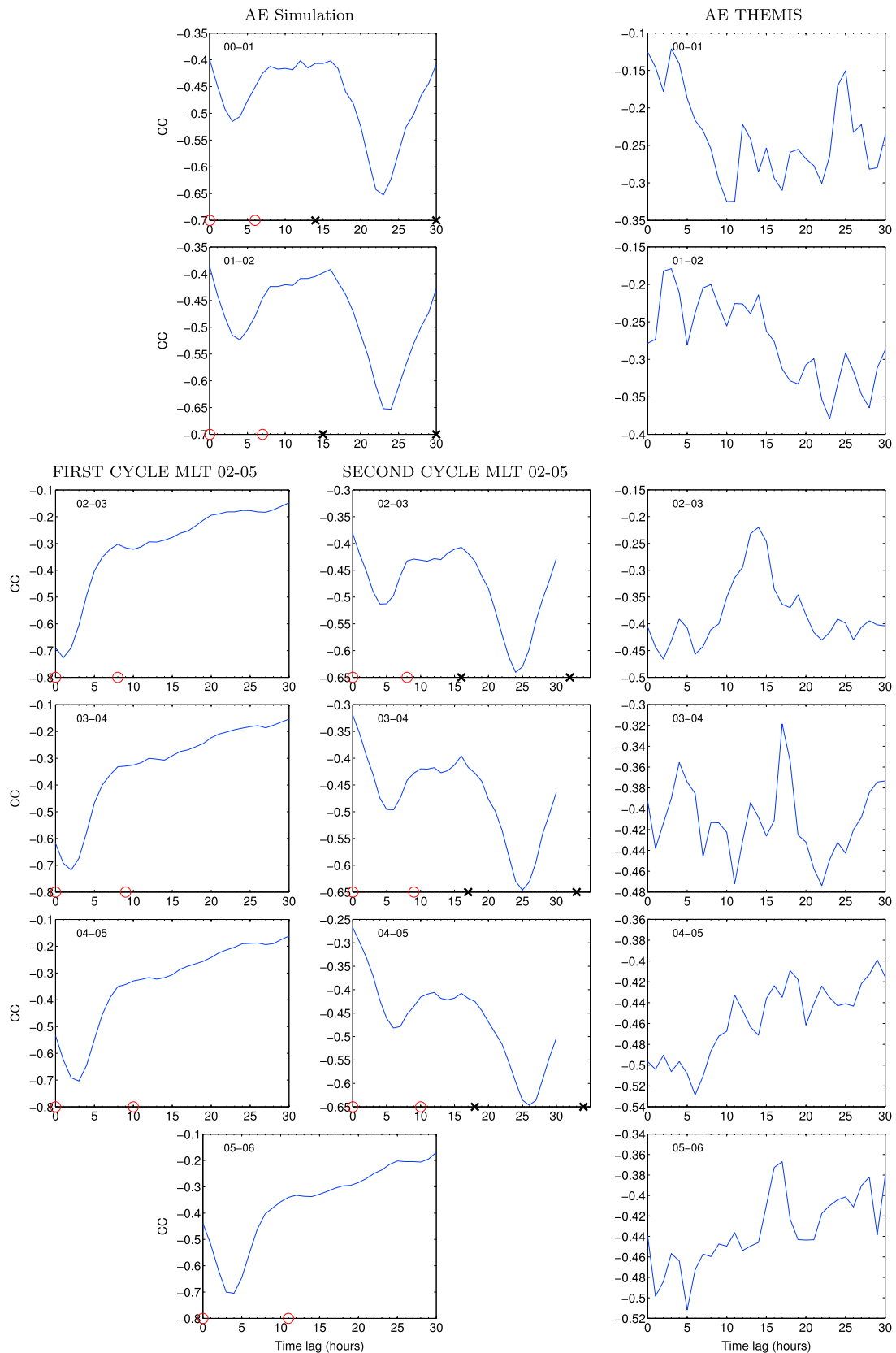


Figure 3. Cross-correlation function describing the $AE-L_{pp}$ relationship for each 1 h MLT bin sector given in the inset. The red circles and black crosses denote the width of the T_{lag} belts. Sectors 01–06 MLT.

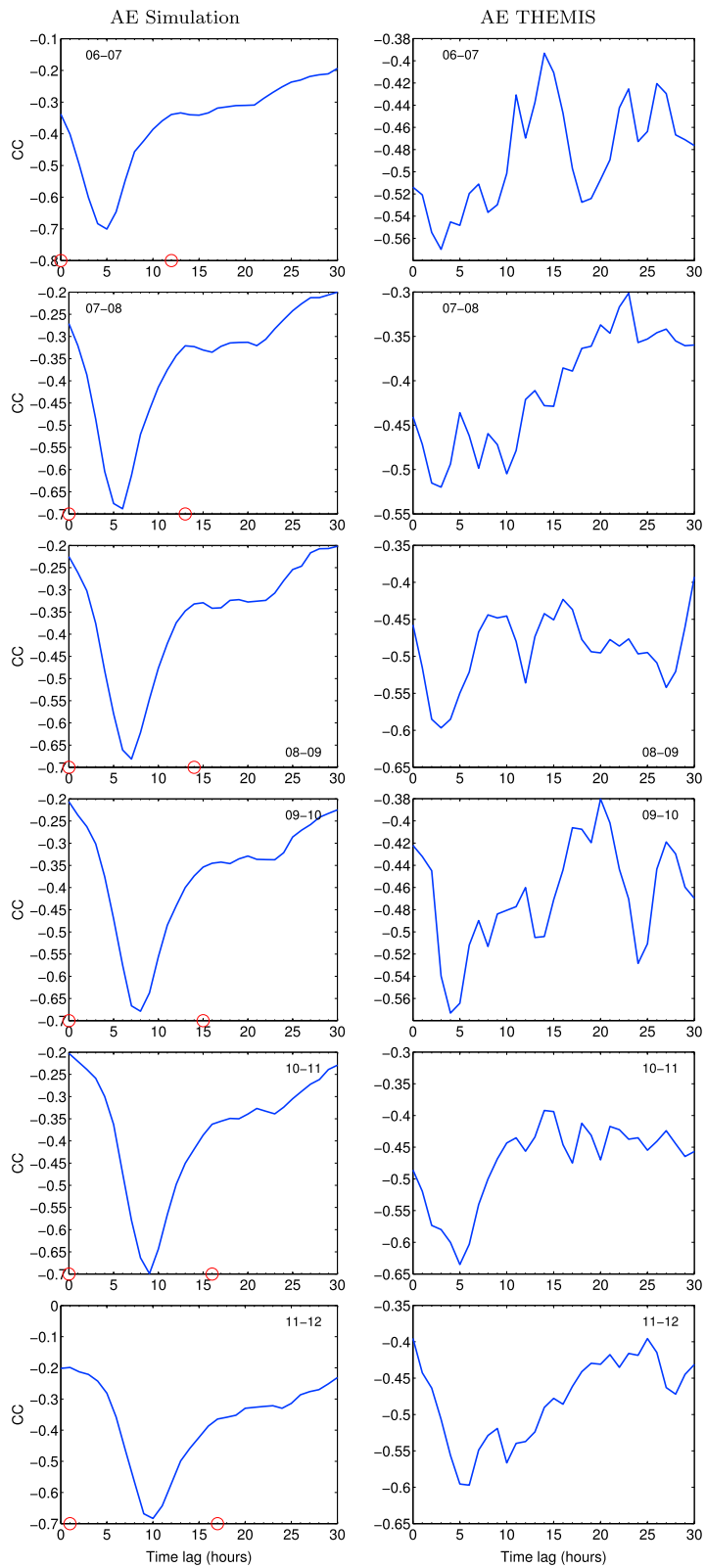


Figure 3. (continued) Sectors 06–12 MLT.

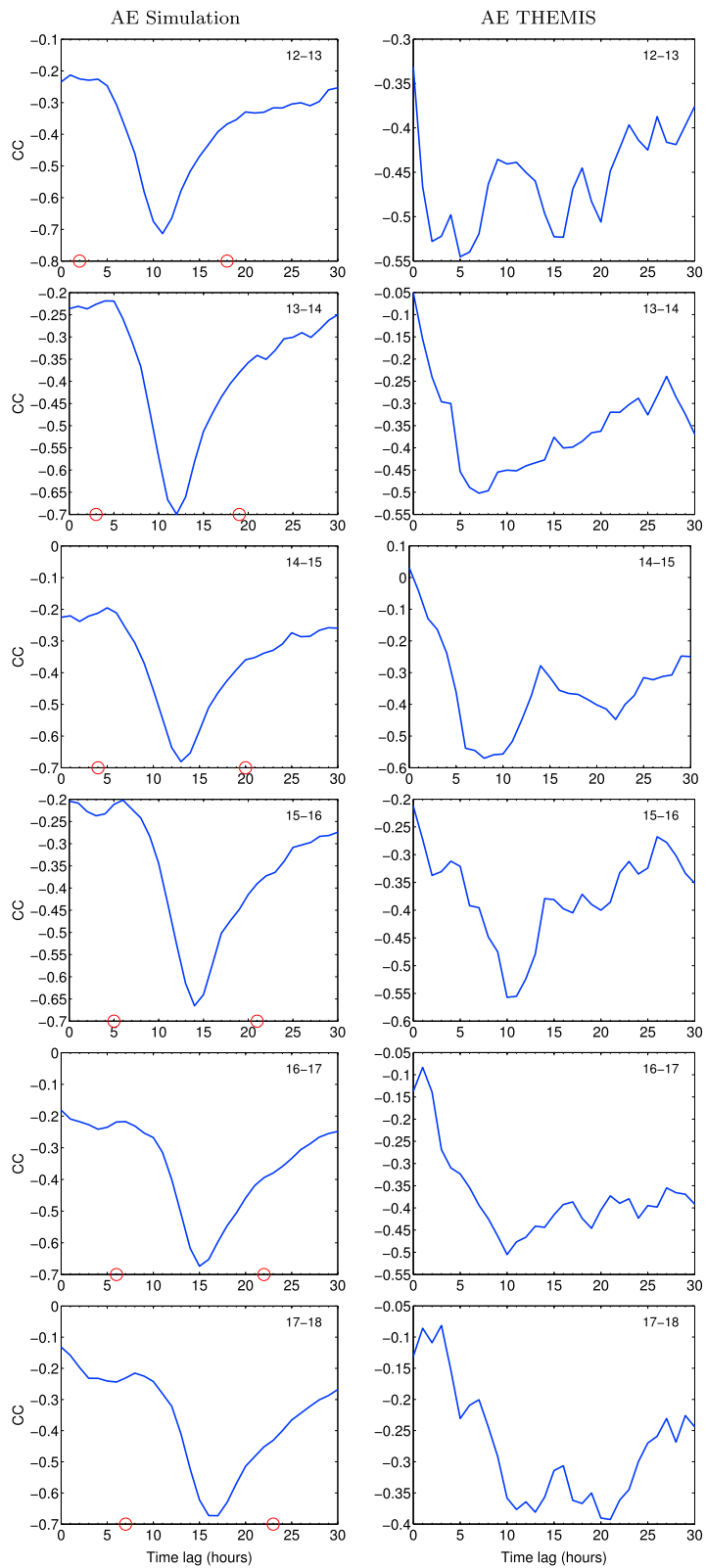


Figure 3. (continued) Sectors 12–18 MLT.

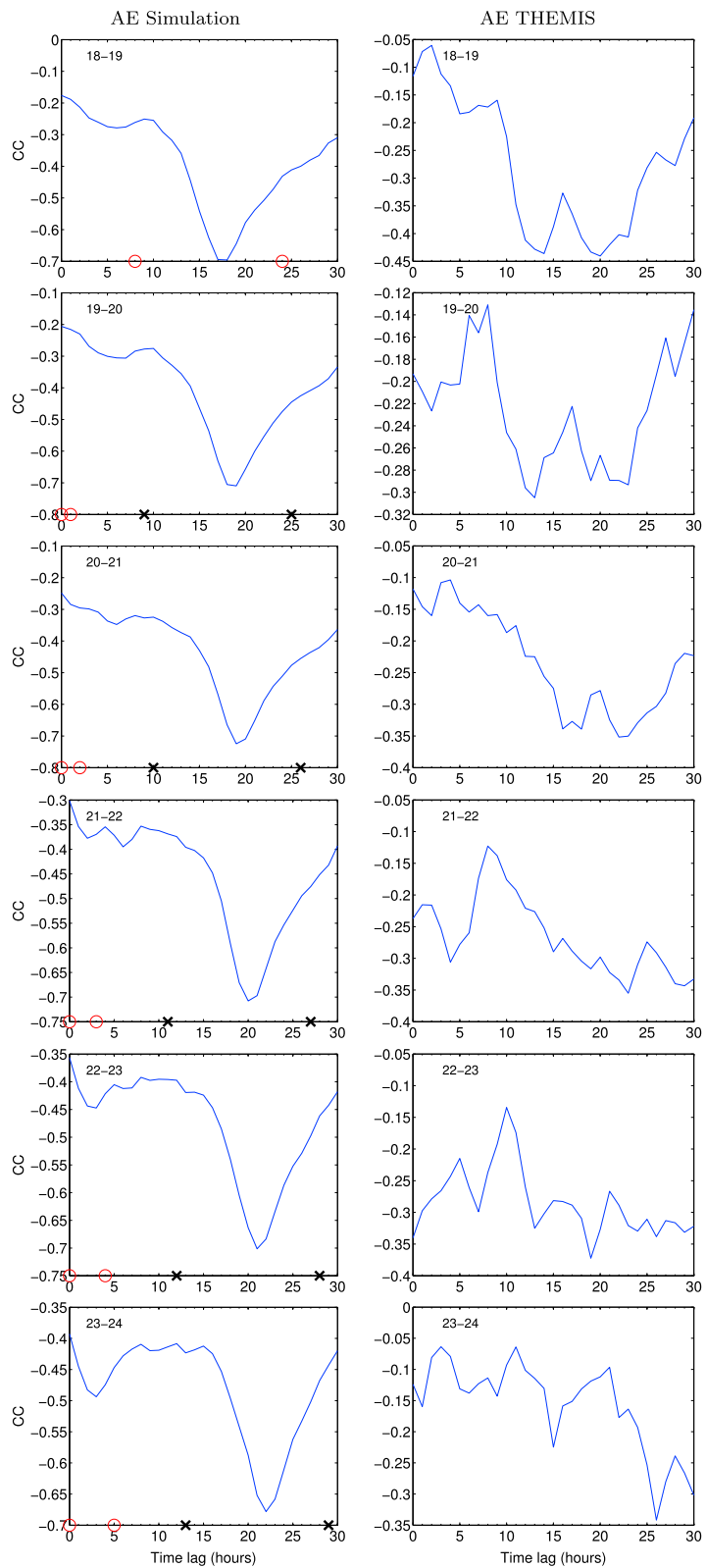


Figure 3. (continued) Sectors 18–24 MLT.

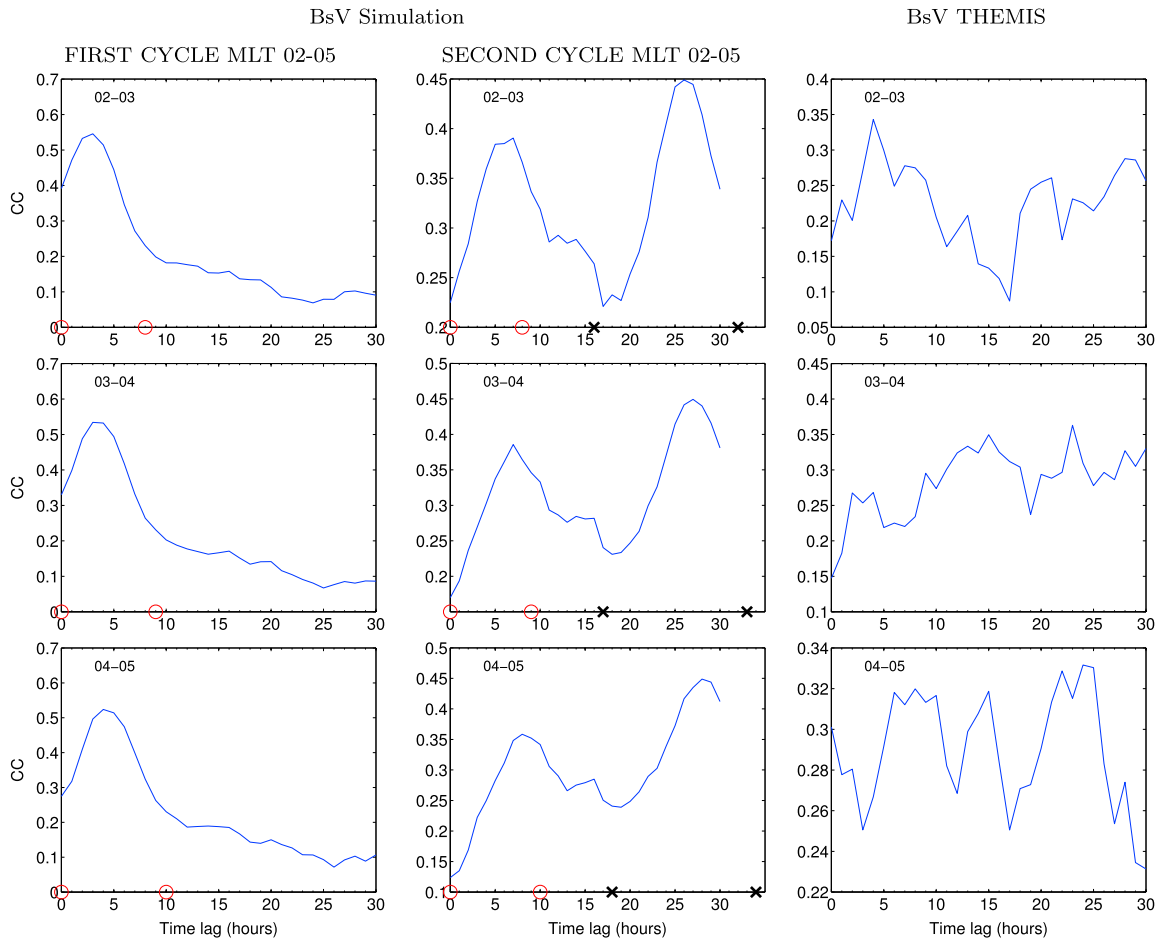


Figure 4. Cross-correlation function describing the $BsV-L_{pp}$ relationship for three 1 h MLT bin sectors given in the inset (02–05 MLT). The red circles and black crosses denote the width of the T_{lag} belts.

$AE-sL_{pp}$ (as an example for geomagnetic-based PP indicators) and $BsV-sL_{pp}$ (as an example for solar wind-based PP indicators) correlations for each 1 h MLT bin sector. For BsV only CC curves related to both first and second simulation cycles are shown to save space.

Generally, the CC curves consist of one or two valleys (or mountains for BsV) and a part with almost constant correlation coefficient with lower values (in an absolute sense) than that of valley/mountain correlation coefficient. The width of valleys/mountains comprises belts of T_{lag} s around the maximal T_{lag} . The importance of these belts is discussed below.

Let us first discuss the CC curves related to AE . In sector 02–03 MLT of the first simulation cycle, the highest correlation (0.7) is obtained at $T_{lag} = 1$. Taking into account that the initial T_{lag} is about an hour or less (Bandić et al., 2017) this indicates the formation of the plasmopause in that sector. The T_{lag} related to the maximal correlation increases with MLTs (e.g., $T_{lag} = 2$ in 03–04 MLT sector, $T_{lag} = 3$ in 04–05 MLT sector, ...). At 21–22 MLT a new peak at low T_{lag} emerges, which then continues to propagate together with the peak at larger T_{lag} up to 05 MLT. This means that the plasmopause formed in the 02–03 MLT sector rotates eastward but also starts to change radially around 21 MLT (at least in a statistical sense), and then this newly formed plasmopause propagates eastward to other MLTs. Note that correlation coefficient at the new peak is lower than that at larger T_{lag} (which amounts for 0.7), and increases from 21 MLT (where amounts for 0.3) to 02–05 MLT (where it amounts for 0.5). This may indicate that 02–05 MLT is the sector where the formation of the new plasmopause takes place with the highest probability, in accordance with Pierrard et al. (2008). The sL_{pps} from the second simulation cycle within 02–05 MLT is the continuation of the first simulation cycle and reflects the plasmopause behavior observed at 21–02 MLT in the first simulation cycle. Therefore, here two valleys/mountains are visible with maximal correlations associated with plasmopause formed after 02–03 MLT

(higher T_{lag}) and plasmopause formed prior to 02–03 MLT (lower T_{lag}). In the second simulation cycle sL_{pp} disappears abruptly at 04–05 MLT, and consequently, in the next sector (05–06 MLT) only one peak at low T_{lag} appears. The observed low T_{lag} s in the first and in the second simulation cycles are not identical (e.g., at 02–03 MLT in the first simulation cycle $T_{lag} = 1$, while in the second $T_{lag} = 4$), revealing that the plasmopause may be formed in a wider MLT range, between about 21 MLT and 05 MLT. The 05 MLT is the latest MLT point of the second simulation cycle, so it may be that the plasmopause is formed in further MLT sectors as well, but cannot be inferred from these simulations.

Now, we can explain the importance of the second simulation cycle in both cases, when Kp (or E field) increases and decreases. If Kp increases, the new plasmopause appears closer to the Earth in the postmidnight sector and the old plasmopause disappears after about 24 h since the plasmasphere is eroded. If Kp decreases, then the new plasmopause is formed at larger radial distances so the vestigial plasmopause (closer to the Earth) formed about 24 h earlier can remain simultaneously with the new one, as sometimes observed. Taking into account that the plasmopause makes also the azimuthal movements (rotation) along with the described radial movements in the postmidnight sector (that occurred within about 24 h), it becomes clear that in both cases, when Kp has increased or decreased, the plasmopause makes at least one rotational cycle (that is, the “lifetime” for this plasmopause). If the plasmopause is formed after 02 MLT (where the simulation starts), e.g., at 04 MLT, then one rotational cycle includes both the first and second simulation cycles. Thus, the second simulation cycle perceives also the information on the formation and is actually the first lifetime cycle in these cases, independently on whether Kp has increased or decreased.

The explained plasmopause evolution can be followed in the snapshots of Figure 1. We start to follow the two-dimensional plasmopause deformation (radial and azimuthal changes) at 16:00 UT of day 2. As Kp increases, the nightside plasmopause starts to move inward (second panel). The radial displacement can be observed in the postmidnight side as indicated by the solid arrow. Throughout the rest of the day (third to the fifth panel), all the nightside plasmopause continued to move inward, since the Kp has further increased. Note that even for small Kp changes (Figure 1, second panel) the plasmopause moved inward at postmidnight (around 02–04 MLT), but Kp had to increase more to cause radial movements at the premidnight side (denoted with dashed arrows in Figure 1, third to fifth panels). Reduction of the nightside plasmopause by about $1 R_E$ is observed. At storm time (Kp greater than 6) larger radial movement is expected. The radial motion is very slight on the dayside. Since the available simulations do not allow to follow individual plasma elements, to examine the azimuthal plasmopause propagation, we identify peak labeled “A.” This peak propagates eastward with the angular velocity close to corotation, indicating the global eastward rotation of the main plasmopause. This rotation can be followed easily on the dayside, but more difficult on the nightside because of the simultaneous radial motions. Note that plasmopause characteristics (e.g., ω_{IM}) observed in individual events can slightly differ from those obtained from the statistical analysis.

As for sL_{pp} -AE, the BsV CC curves at 02–05 MLTs of the second simulation cycle show two correlation peaks at low and high T_{lag} s. The low T_{lag} s from the first and from the second simulation cycles differ, again providing information on the MLT range in which the plasmopause is formed. Note that T_{lag} s obtained for BsV are about 1–2 h larger than for AE, indicating that L_{pp} responds quicker to AE than to BsV . This can be understood as follows. Both L_{pp} and AE change due to BsV . The delay of AE with respect to BsV is expected since differing lag times between the various PP indicators have been reported (e.g., Fung & Shao, 2008; Verbanac et al., 2011). Therefore, the T_{lag} s for L_{pp} - BsV and L_{pp} -AE are likely different. The correlations are also slightly lower for BsV than for AE.

We note that the simulation starting point influences the absolute value of T_{lag} s. Nevertheless, the obtained T_{lag} s indicate the MLT sectors of formation and provide information on the plasmopause propagation.

To examine the meaning of the T_{lag} belts, let us consider the 10–11 MLT sector. The determined T_{lag} is 9 h. As pointed out above it is possible that the plasmopause is also formed after 05 MLT, for example, at 06 MLT as obtained when Weimer E field model is used (Pierrard et al., 2008) or at 07 MLT obtained from past THEMIS eL_{pp} analyses (Bandić et al., 2017). Let us suppose now that plasmopause is formed somewhere between 21 MLT and 07 MLT. Larger T_{lag} is expected at 10–11 MLT if the plasmopause is formed at 21 MLT than if it is formed at 07 MLT. This exactly reflects the T_{lag} belt around the maximal T_{lag} of 9 h. If we suppose that the plasmopause is transmitted with $\omega_{IM} = 1$, then we expect T_{lag} s around 13 h or around 3 h depending if the formation was triggered at 21 MLT or at 07 MLT. Taking further into account that the deformation likely comprises a few MLTs simultaneously (Bandić et al., 2017; Goldstein, Burch, et al., 2005; Pierrard & Lemaire, 2004), for instance, 3 MLTs,

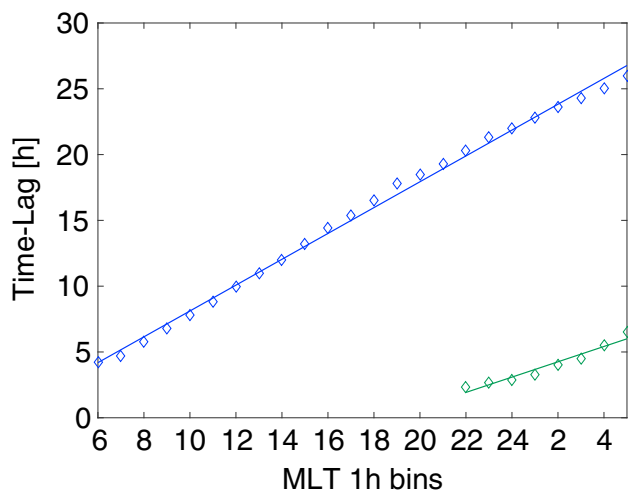


Figure 5. T_{lag} -MLT dependence for AE. The points belonging to the MLT intervals are associated to the end of the interval (for instance 6 indicates the 1h-bin 05-06 MLT). The blue symbols denote global (the highest) maxima in the CC curves. The green symbols denote local (the second highest) maxima that emerge at 21–22 MLT and last up to 04–05 MLT.

the observed T_{lag} can be even less than 3 h. A wider belt of T_{lag} s with values between 0 and 16 h is therefore expected. In each MLT sector, the widths of the T_{lag} belts are calculated as explained above and are indicated by red circles and black crosses in Figures 3 and 4. Since the sL_{pp} - BsV CC curves are about 1–2 h shifted toward the larger T_{lag} values with respect to the sL_{pp} - AE CC curves, these circles and crosses should be accordingly shifted in Figure 4. However, in order to visualize the time delay between these two PP indicators, we did not shift them. Interestingly, with the employed time-lag method we were able to deduce that the erosion can take place between 21 and 07 MLT, although the simulations used the E5D E field. Namely, the E5D E field is the strongest between 02 MLT and 04 MLT (Pierrard et al., 2008) allowing the interchange instability to penetrate down to lowest radial distance and favoring the plasmopause formation at these MLTs.

As shown in the first column of Figure 3 the valley/mountain and the associated T_{lag} belt start to detach from the origin (constant part of CC curve with lower correlation coefficient appearing at the left part of the valley) at about 10 MLT and the width of the T_{lag} belt remains nearly constant up to 21 MLT. This width amounts for the MLT range of formation sectors plus about a few sectors accounting for deformation of several MLTs at the same time. This is exactly what we expect assuming propagation of the plasma-

pause with $\omega_{IM} = 1$. Although the simulation starts at 02 MLT and left part of the valley sticks to the origin up to about 10 MLT, the widening of the T_{lag} belt to the right reflects the effect of the T_{lag} s accumulation. Thus, considering the width of the T_{lag} belts even from the first simulation cycle, we conclude that the formation was before 02 MLT. In the MLT sectors where the plasmopause is not only propagating but is also formed, two T_{lag} belts with different widths are observed in CC curves related to the second simulation cycle. The width around the lower T_{lag} widens with MLT (from the MLT of the formation) and the width around the higher T_{lag} remains constant. Although different maximal T_{lag} values related to the lower T_{lag} are observed in the first and second simulation cycles, the corresponding T_{lag} belts have the same width, suggesting the plasmopause propagation speed of $\omega_{IM} \sim 1$. On the other side, calculating ω_{IM} from equation (1) using the determined highest correlation coefficient T_{lag} s, we obtain two propagation velocity branches within 22–05 MLT, as shown in Figure 5. The MLT coordinates are labeled by the end of the 1 h MLT bins (for instance, 22 MLT indicates the 1 h bin MLT 21–22). The values at 03 MLT, 04 MLT, and 05 MLT plotted in both velocity lines are taken from the second simulation cycle. The slopes of these curves indicate $\omega_{IM} = 1$ and $\omega_{IM} \sim 2$. The higher value of ω_{IM} associated to the lower T_{lag} s is because the maximal T_{lag} increases slower ($\Delta T_{lag} \sim 4$ in sector 7 MLT wide) than the maximal T_{lag} related to the higher T_{lag} s ($\Delta T_{lag} \sim 1$ in sector 1 MLT wide). For other PP indicators, we obtain mean angular velocity very close to those obtained for AE.

We note that the discussed numerical values of the MLT ranges of the formation sectors, T_{lag} s and the estimated width of the T_{lag} belts are obtained from statistical analyses of a large number of sL_{pp} s, and have to be taken as the most probable ones. Taking further into account that probably different MLT sectors are deformed simultaneously (affected by formation) in individual events embraced by our statistical sample, the influence of the simulation starting point, and the 1 h data resolution, it is clear that we cannot determine these values exactly.

5. MLT Dependence of THEMIS-Based Plasmopause and Comparison With Theoretical Results

The MLT propagation effects and other plasmopause characteristics inferred from THEMIS-based eL_{pp} s are presented in Bandić et al. (2017). Here we show and discuss the behavior of the CC curves (presented in Figures 3 and 4, last column) and compare them with those obtained from the simulations (first column or first two columns for sectors 02–05 MLTs in Figures 3 and 4).

Although there are enough data in each 1 h bin MLT sector, the oscillatory nature of the CC curves indicates that even more data per sector is needed to obtain smooth curves, such as in the case of CC curves derived from simulations. Further, we recall that we do not have the sequential time series, for example,

the plasmopause snapshots within each day. This also contributes to the oscillatory nature of the experimental CC curves. At simulations, the model results are binned by the input E field E5D model (characterized by the Kp index). Therefore, the simulation CC curves derived from these data are smoother. In some of premidnight and postmidnight MLTs, experimental CC curves with double peak structure are recognized. These curves are also the most oscillatory ones, likely indicating the effects of complex physical processes there. In our statistical sample some of these MLT sectors contain dominantly newly formed $eL_{pp}s$, while others a larger ratio of $eL_{pp}s$ formed one cycle before, and consequently, one of the peaks, at low T_{lag} or at large T_{lag} , prevails and then the two peak structure is blurred. CC curves with clear one peak structure are observed in the dayside, dusk, and postdusk sectors. Generally, this peak moves to larger T_{lag} from ~ 08 MLT up to ~ 21 MLT indicating the eastward plasmopause rotation. At about 21 MLT the second peak at low T_{lag} appears, suggesting the new plasmopause formation. This is in accordance with the study by Bandić et al. (2017) which has suggested the plasmopause formation between 23 and 07 MLT. Here by inspecting the CC curves in more detail, we further recognize the importance of the peak at low T_{lag} that appears at 21 MLT.

We note that CC curves obtained using different PP indicators (other than the shown AE and BsV curves) have generally similar behavior and provide the same conclusions. This will be discussed further below.

Generally, CC curves related to THEMIS $eL_{pp}s$ and to simulated $sL_{pp}s$ show similar trends and are in accordance in the following: (a) the highest correlation $T_{lag}s$ are shifted to larger values moving away from the formation MLT sector; (b) double peaks are seen from premidnight, starting at about ~ 21 MLT, to dawn. Thus, CC curves from both data sets indicate that from dawn to premidnight plasmopause only propagates, and that from ~ 21 MLT to dawn plasmopause propagates but is also formed. Although the simulations stop at 05 MLT, the width of the T_{lag} belt in the simulation CC curve at about 10 MLT indicates that the formation may be triggered up to 07 MLT, similarly to the results of Bandić et al. (2017) from the same THEMIS data set. Here because of the oscillatory nature of the experimental CC curve, we were not able to determine the width of T_{lag} belts. Nevertheless, the curve does not detach from the origin before ~ 10 MLT, indicating that the formation took place up to 07 MLT. Thus, the experimental CC curves detach from the origin similarly to the simulation-based ones. The resemblance of the experimental and simulation CC curves is much better in sectors identified as propagational ones (07–21 MLT). Recall that simulated $sL_{pp}s$ from the first and second simulation cycles are analyzed separately and thus two different CC curves are obtained between 02 MLT and 05 MLT. In these MLT sectors, THEMIS data set contains both newly formed $eL_{pp}s$ and those formed one cycle before. Thus, the experimental curves in 02–05 MLT sectors may be understood as the combination of the first and second simulation cycle curves.

Note that the T_{lag} peaks in simulation and experimental CC curves are not exactly at the same MLTs. The reasons may be the influence of the simulation starting time on the absolute values of $T_{lag}s$ and/or different mean propagation speed of simulated and THEMIS plasmopause. Namely, in simulations $\omega_{IM} = 1$ always, while from THEMIS $eL_{pp}s$ Bandić et al. (2017) derived two different propagation speeds (1.10 in the 07–15 MLT, 0.45 in the 15–23 MLT sector. The velocity in the 23–07 MLT sector could not be uniquely determined; however, it was indicated that the erosion propagates quite fast in these MLT sectors).

To show that CC curves obtained using different PP indicators have a similar pattern, in Figure 6 we present CC curves for three MLT sectors (11–12 MLT, 18–19 MLT, and 02–03 MLT) and all considered PP indicators. These three MLT sectors are representative for day, dusk, and postmidnight sides. For a better comparability, all CC curves are shown at the same scale. Thick blue and red lines are related to the simulations and observations, respectively. Generally, we can recognize similar trends of both simulation and experimental CC curves, with sometimes displaced peaks in MLT. The curves track each other somewhat better from dawn to premidnight MLTs. As already noted, in sectors other than these MLTs, THEMIS data set contains both new plasmopause and those formed one cycle before, and likely more vestigial ones in the events characterized by Kp decrease. The latter is the consequence of the method employed to identify the $eL_{pp}s$. Namely, if the innermost sharp gradient is considered as the criterion for the plasmopause (Bandić et al., 2017; Cho et al., 2015) having a lifetime comparable to the refilling time, then probably more $eL_{pp}s$ corresponding to second simulation cycles are identified. Thus, the discrepancy between simulation-based and experimental CC curves is expected.

To investigate how the profile of the CC curves are influenced by the number of used $sL_{pp}s$, we repeated the simulations with less data points. We start with the initial simulated data set. Then, in each 1 h MLT sector, we randomly choose the same number of $sL_{pp}s$ as available from THEMIS in that sector. The procedure is repeated and new data set with less data points is created. CC curves obtained from the reduced data sets are shown

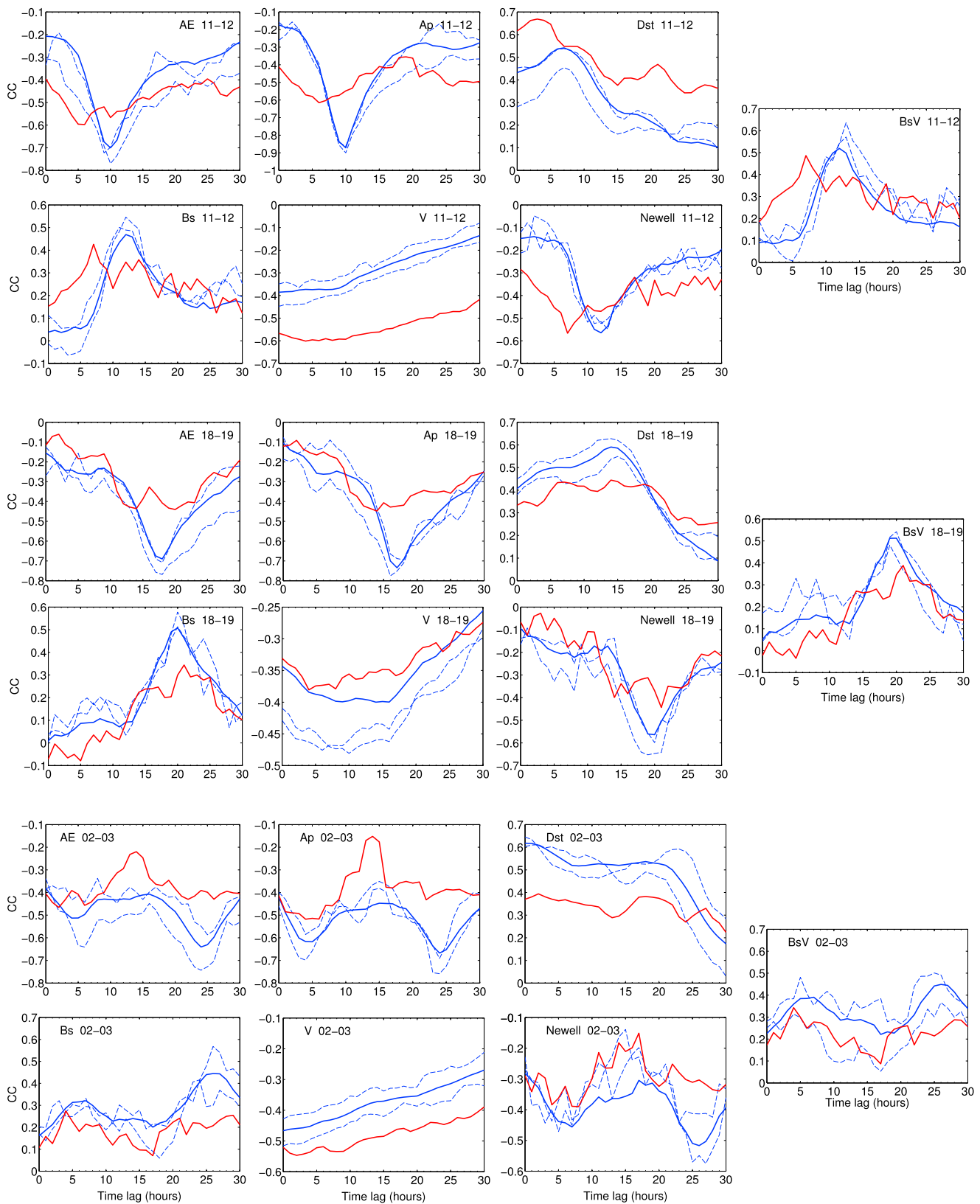


Figure 6. Cross-correlation functions at 11–12 MLT, 18–19 MLT, and 02–03 MLT sectors obtained using different PP indicators. Thick blue and red lines are related to the simulations and observations, respectively. CC curves obtained from the reduced simulation-based data sets are shown as dashed blue lines. See text for details.

in Figure 6 as dashed blue lines. These dashed curves are not smooth anymore and begin showing an oscillatory pattern similar to the experimental ones. Their CC profiles are again similar to those from THEMIS (solid red curve), and to those obtained with the initial simulated data set (solid blue curve). Note that the two dashed curves have the same trend, but they do not overlap. We additionally perform an analysis to estimate the confidence interval (thereafter $\text{std}(\text{CC})$) of the correlation values for the initial, reduced, and experimental data sets to characterize their uncertainties. We use the calculation presented in Kwan (2009). Correlation values related to the initial simulated data set have lower uncertainty than those obtained with both reduced and experimental data sets. For all data sets, the uncertainty decreases with increasing correlation. Therefore, the range of $\text{std}(\text{CC})$ values is estimated separately for the constant part of the CC curves and for the part of the CC curves around maximal CC values. Considering all PP indicators for the maximum part of the CC curves the $\text{std}(\text{CC})$ ranges related to the initial simulated, reduced simulated, and experimental data sets are 0.01–0.02, 0.03–0.05, and 0.03–0.05, respectively. The corresponding $\text{std}(\text{CC})$ ranges for the constant part of the CC curves are 0.03–0.05, 0.06–0.08, and 0.04–0.08. The mentioned orders of uncertainties are representative for all MLT sectors. These values confirm that although THEMIS data set contains a respectable number of eL_{pp} s, there is still not enough data in each 1 h MLT bin to obtain the smooth curve which would represent the final CC curve.

6. Discussion

In this study, we have investigated and compared the global plasmopause characteristics obtained from THEMIS observations with those inferred from simulations based on interchange instability mechanism.

We found that the main observed plasmopause features, as eastward plasmopause rotation and formation in MLT sectors are well reproduced by the simulations. Moreover, the radial extension of the mean eL_{pp} and mean sL_{pp} values in each MLT sector differ only slightly. Therefore, the results obtained from the model simulations help us to interpret the observations.

It is important to note that different PP indicators show very similar plasmopause behavior. Some specific plasmopause structures may possibly move differently in individual events (e.g., westward as inferred from IMAGE EUV plasmopause Goldstein, Sandel, et al., 2005), and statistically, such local movements are not seen.

We recognize the importance of the T_{lag} belts, which additionally indicate the MLT range of the plasmopause formation and also the mean angular velocity of the plasmopause propagation. The oscillatory nature of the THEMIS-based CC curves does not allow to precisely determine the width of the T_{lag} belts. Therefore, we analyze these widths using simulated CC curves. Considering the width of the T_{lag} belts and the MLT position of the valley/mountain in the CC curves, we concluded that the formation may be triggered up to about 07 MLT, in accordance with Bandić et al. (2017).

The experimental results indicate that erosion likely starts at about 21 MLT. IMAGE EUV plasmopause observed in the individual event on 17 April 2002 Goldstein, Burch, et al., (2005) also suggest that plasmopause may be formed in the premidnight MLTs. Simulation results support these observations. Note that on the other side, many previous works based on interchange instability simulations (Lemaire & Pierrard, 2008; Pierrard & Cabrera, 2006) and satellite observations (Bandić et al., 2016, 2017; Goldstein, Sandel, et al., 2005; Verbanac et al., 2015) have emphasized the formation in the postmidnight MLT sectors only. Thus, it is worth to investigate this issue further.

Using the highest correlation T_{lag} s, Bandić et al. (2017) derived that the plasmopause propagates with velocity very close to the corotation in the 07–15 MLT sector and much slower in the 15–23 MLT sector. They indicated the possibility of fast erosion propagation within 23–07 MLT. Bandić et al. (2016) have also reported that the plasmopause derived from CRRES satellite likely propagates at the higher rate than the corotation in the postmidnight side. As regards THEMIS-based plasmopause, Bandić et al. (2017) calculated the mean angular propagation speed considering T_{lag} differences for sectors that are 8 h bins wide (e.g., difference between T_{lag} at 23 MLT and T_{lag} at 15 MLT). We suggest that the scatter around the trend MLT- T_{lag} curve in 15–23 MLT sector (see their Figure 1, bottom panel) may lead to overestimation of the T_{lag} differences and thus to the underestimation of the propagation speed. Within 23–07 MLT the oscillations in MLT- T_{lag} curve are very prominent (see their Figure 1), because they consider sometimes peak at low T_{lag} , sometimes at high T_{lag} , depending which one prevails. From the lower identified branch in their Figure 1, bottom panel (see encircled branches) one can estimate that the mean angular speed is larger than 2 ($\Delta T_{lag} = 3$ in sector 8 MLT wide). This is in agreement

with the largest velocity that we estimated within 22–05 MLT sector based on simulated plasmopause. After considering the importance of T_{lag} belt widths we conclude that this velocity is indeed not a realistic one since the analysis of these widths indicates that the main plasmopause rotates eastward with the mean angular speed that corresponds to the Earth's rotational speed. Therefore, we suggest that the THEMIS-based plasmopause also likely corotates with the Earth within 23–07 MLT sector. This issue has to be further investigated and validated using more experimental data with better UT-MLT coverage than the data set used by Bandić et al. (2017). Such further study can also help in resolving whether the single peak in sectors other than 21–07 MLT is caused by the fast angular propagation speed in the postmidnight sector as proposed by Bandić et al. (2017) or not.

Works by Verbanac et al. (2015) and Bandić et al. (2016, 2017) based on different satellite measurements have all indicated that interchange instability is likely responsible for many observed plasmopause characteristics. The present study comparing eL_{pps} and sL_{pps} validates their indication and additionally revises the most important plasmopause characteristics, as the MLT range of formation and angular propagation. However, this does not mean that other physical processes are not important for the plasmopause dynamics. In this regard, it is worth concluding that further investigations are recommended.

7. Conclusions

Statistical comparison of the global behavior of the experimental (THEMIS based) and simulated plasmopause (based on interchange instability mechanism) is performed, analyzed, and interpreted for the first time. We focused on plasmopause formation and propagation characteristics. The simulation results are used to support the interpretation of the observations.

We recall on noting the differences from previous studies which have also employed simulations based on interchange instability mechanism (e.g., Pierrard & Lemaire, 2004; Pierrard & Cabrera, 2005, 2006) and those that have used LCS simulations (e.g., Goldstein, Burch, et al., 2005; Goldstein, Sandel, et al., 2005). In these past works, the plasmopause shapes obtained with simulations are compared with those observed with IMAGE EUV in single events only. In such snapshots comparisons, the efforts were mostly done to reproduce some of the observed plasmopause structures (e.g., plumes, shoulders). Images often do not have the complete MLT coverage at each UT due to noise or sunlight contamination and therefore the motion of the whole main plasmopause could not be followed. Only motion of the restricted plasmopause extension or of some plasmopause structure was possible to be tracked. The deduced motions are representative only for the particular single case. On the other side, in this study, we have analyzed plasmopause positions from many events within the period July 2008 to December 2012. In such a way we have derived the statistical characteristics of the main plasmopause which represent the most probable global plasmopause behavior.

The observations suggest a general eastward azimuthal plasmopause propagation and a radial plasmopause motion restricted to 21–07 MLT. The erosion likely takes place simultaneously at a range of MLTs. The simulation results show the same plasmopause behaviors. Thus, they can help to better understand the physics behind the observed features of plasmasphere dynamics. Closest analysis indicates that any changes of the magnetospheric E field (Kp changes) will cause the erosion of the plasmopause in the postmidnight sector, around 02–05 MLT. Only stronger changes of the E field lead to the formation of the plasmopause at pre-midnight or around dawn. This can be interpreted as follows. Both the E5D electric field and the interchange velocity are the highest in the postmidnight MLT sectors maximizing the erosion of the plasmopause in these MLTs. Thus, the formation of the new plasmopause at postmidnight is the most probable. On the dayside, plasmopause moves almost entirely azimuthally. The analysis further indicates that the plasmopause at all MLTs azimuthally propagates with the mean angular velocity close to corotation, at least for lower geomagnetic activity periods. This has to be further investigated with more experimental data with as high as possible MLT-UT coverage.

Although our study suggests that the experimental plasmopause characteristics are in accordance with the interchange instability mechanism, to definitively conclude which physical mechanism is the right one or the most important for the plasmopause formation further investigations should be done.

The present study contributes to resolving some of the long-lasting, unresolved issues related to plasmaspheric erosion and plasmopause dynamics.

Acknowledgments

The authors thank the space weather portal for providing the plasmasphere model and Giovanni Piredda for helpful discussion. Plasmapause positions are obtained from THEMIS measurements accessible at <http://themis.ssl.berkeley.edu>. The authors further thank all the staff members providing the geomagnetic indices available at <https://www.ngdc.noaa.gov> and <http://wdc.kugi.kyoto-u.ac.jp>, and the solar wind parameters available at <http://www.srl.caltech.edu/ACE>. V. Pierrard thanks the Solar Terrestrial Center of Excellence and the Belgian Federal Policy for the interuniversity project P7/08 CHARM.

References

- Bandić, M., Verbanac, G., Moldwin, M. B., Pierrard, V., & Piredda, G. (2016). MLT dependence in the relationship between plasmapause, solar wind, and geomagnetic activity based on CRRES: 1990–1991. *Journal of Geophysical Research: Space Physics*, *121*, 4397–4408. <https://doi.org/10.1002/2015JA022278>
- Bandić, M., Verbanac, G., Pierrard, V., & Cho, J. (2017). Evidence of MLT propagation of the plasmapause inferred from THEMIS data. *Journal of Atmospheric and Solar-Terrestrial Physics*, *161*, 55–63. <https://doi.org/10.1016/j.jastp.2017.05.005>
- Carpenter, D. L., & Anderson, R. R. (1992). An ISEE/whistler model of equatorial electron density in the magnetosphere. *Journal of Geophysical Research*, *97*(A2), 1097–1108.
- Chen, A. J., & Wolf, R. A. (1972). Effects on the plasmasphere of time varying convection electric field. *Planetary and Space Science*, *20*, 483–509. [https://doi.org/10.1016/0032-0633\(72\)90080-3](https://doi.org/10.1016/0032-0633(72)90080-3)
- Cho, J., Lee, D.-Y., Kim, J.-H., Shin, D.-K., Kim, K.-C., & Turner, D. (2015). New model fit functions of the plasmapause location determined using THEMIS observations during the ascending phase of Solar Cycle 24. *Journal of Geophysical Research: Space Physics*, *120*, 2877–2889. <https://doi.org/10.1002/2015JA021030>
- Fung, S. F., & Shao, X. (2008). Specification of multiple geomagnetic responses to variable solar wind and IMF input. *Annales Geophysicae*, *26*, 639–652. <https://doi.org/10.5194/angeo-26-639-2008>
- Gallagher, D. L., Adrian, M. L., & Liemohn, M. W. (2005). Origin and evolution of deep plasmaspheric notches. *Journal of Geophysical Research*, *110*, A09201. <https://doi.org/10.1029/2004JA010906>
- Goldstein, J., Burch, J. L., Sandel, B. R., Mende, S. B., C. Son Brandt, P., & Hairston, M. R. (2005). Coupled response of the inner magnetosphere and ionosphere on 17 April 2002. *Journal of Geophysical Research*, *110*, A03205. <https://doi.org/10.1029/2004JA010712>
- Goldstein, J., Sandel, B., Forrester, W., Thomsen, M., & Hairston, M. (2005). Global plasmasphere evolution 22–23 April 2001. *Journal of Geophysical Research*, *110*, A12218. <https://doi.org/10.1029/2005JA011282>
- Goldstein, J., Sandel, B. R., Hairston, M., & Reiff, P. H. (2003). Control of plasmaspheric dynamics by both convection and sub-auroral polarization stream. *Geophysical Research Letters*, *30*(24), 2243. <https://doi.org/10.1029/2003GL018390>
- Goldstein, J., Spiro, R., Reiff, P., Wolf, R., Sandel, B., Freeman, J., & Lambour, R. (2002). IMF-driven overshielding electric field and the origin of the plasmaspheric shoulder of May 24, 2000. *Geophysical Research Letters*, *29*, 1819. <https://doi.org/10.1029/2001GL014534>
- Horwitz, J. L., Comfort, R. H., & Chappell, C. R. (1990). A statistical characterization of plasmasphere density structure and boundary locations. *Journal of Geophysical Research*, *95*, 7937–7947. <https://doi.org/10.1029/JA095IA06p07937>
- Kwan, C. C. Y. (2009). Estimation error in the correlation of two random variables: A spreadsheet-based exposition. *Spreadsheets in Education (eJSiE)*, *3*(2), Article 2.
- Kwon, H. J., Kim, K. H., Jee, G., Park, J. S., Jin, H., & Nishimura, Y. (2015). Plasmapause location under quiet geomagnetic conditions (K_p less than 1): THEMIS observations. *Geophysical Research Letters*, *42*, 7303–7310. <https://doi.org/10.1002/2015GL066090>
- Lemaire, J., & Kowalkowski, L. (1981). The role of plasma interchange motion for the formation of a plasmapause. *Planetary and Space Science*, *29*, 469–478. [https://doi.org/10.1016/0032-0633\(81\)90090-8](https://doi.org/10.1016/0032-0633(81)90090-8)
- Lemaire, J., & Pierrard, V. (2008). Comparison between two theoretical mechanisms for the formation of the plasmapause and relevant observations. *Geomagnetism and Aeronomy*, *48*(5), 553–570. <https://doi.org/10.1134/S0016793208050010>
- Lemaire, J. F., & Gringauz, K. I. (1998). *The Earth's plasmasphere*. New York: Cambridge University Press.
- Liu, X., & Liu, W. (2014). A new plasmapause location model based on THEMIS observations. *Science China Earth Sciences*, *57*, 2552–2557.
- Liu, X., Liu, W., Cao, J. B., Fu, H. S., Yu, J., & Li, X. (2015). Dynamic plasmapause model based on THEMIS measurements. *Journal of Geophysical Research: Space Physics*, *120*, 10,543–10,556. <https://doi.org/10.1002/2015JA021801>
- McIlwain, C. E. (1986). A K_p dependent equatorial electric field model. *Advances in Space Research*, *6*(3), 187–197. [https://doi.org/10.1016/0273-1177\(86\)90331-5](https://doi.org/10.1016/0273-1177(86)90331-5)
- Moldwin, M. B., Downward, L., Rassoul, H. K., Amin, R., & Anderson, R. R. (2002). A new model of the location of the plasmapause: CRRES results. *Journal of Geophysical Research*, *107*(A11), 1339. <https://doi.org/10.1029/2001JA009211>
- Murakami, G., Yoshioka, K., Yamazaki, A., Nishimura, Y., Yoshikawa, I., & Fujimoto, M. (2016). The plasmapause formation seen from meridian perspective by KAGUYA. *Journal of Geophysical Research: Space Physics*, *121*, 11,973–11,984. <https://doi.org/10.1002/2016JA023377>
- Newell, P. T., Sotirelis, T., Liou, K., Meng, C.-I., & Rich, F. J. (2007). A nearly universal solar wind-magnetosphere coupling function inferred from 10 magnetospheric state variables. *Journal of Geophysical Research*, *112*, A01216. <https://doi.org/10.1029/2006JA012015>
- O'Brien, T. P., & Moldwin, M. B. (2003). Empirical plasmapause models from magnetic indices. *Geophysical Research Letters*, *30*(4), 1152. <https://doi.org/10.1029/2002GL016007>
- Pierrard, V., & Cabrera, J. (2005). Comparisons between EUV/IMAGE observations and numerical simulations of the plasmapause formation. *Annales Geophysicae*, *23*(7), 2635–2646. <https://doi.org/10.5194/angeo-23-2635-2005>
- Pierrard, V., & Cabrera, J. (2006). Dynamical simulations of plasmapause deformations. *Space Science Reviews*, *122*(1–4), 119–126. <https://doi.org/10.1007/s11214-005-5670-8>
- Pierrard, V., & Lemaire, J. (2004). Development of shoulders and plumes in the frame of the interchange instability mechanism for plasmapause formation. *Geophysical Research Letters*, *31*, L05809. <https://doi.org/10.1029/2003GL018919>
- Pierrard, V., Khazanov, G. V., Cabrera, J., & Lemaire, J. (2008). Influence of the convection electric field models on predicted plasmapause positions during magnetic storms. *Journal of Geophysical Research*, *113*, A08212. <https://doi.org/10.1029/2007JA012612>
- Pierrard, V., & Stegen, K. (2008). A three-dimensional dynamic kinetic model of the plasmasphere. *Journal of Geophysical Research*, *113*, A10209. <https://doi.org/10.1029/2008JA013060>
- Sandel, B. R., Goldstein, J., Gallagher, D. L., & Spasojevic, M. (2003). Extreme ultraviolet imager observations of the structure and dynamics of the plasmasphere. *Space Science Reviews*, *109*, 25–46. <https://doi.org/10.1023/B:SPAC.0000007511.47727.5b>
- Sheeley, B. W., Moldwin, M. B., Rassoul, H. K., & Anderson, R. R. (2001). An empirical plasmasphere and trough density model: CRRES observations. *Journal of Geophysical Research*, *106*, 25,631–25,642. <https://doi.org/10.1029/2000JA000286>
- Verbanac, G., Pierrard, V., Bandić, M., Darrouzet, F., Rauch, J.-L., & Décréau, P. (2015). Relationship between plasmapause, solar wind and geomagnetic activity between 2007 and 2011. *Annales Geophysicae*, *33*, 1271–1283. <https://doi.org/10.5194/angeo-33-1271-2015>
- Verbanac, G., Vršnak, B., Živković, S., Hojsak, T., Veronig, A. M., & Temmer, M. (2011). Solar wind high-speed streams and related geomagnetic activity in the declining phase of solar cycle 23. *Astronomy and Astrophysics*, *533*, A49–1–A49–6. <https://doi.org/10.1051/0004-6361/201116615>